Liquid-Phase Peak Force Infrared Microscopy for Chemical Nano-Imaging and Spectroscopy

Haomin Wang,[1] Joseph M. González-Fialkowski,[1] Wenqian Li,[2] Qing Xie,[1] Yan Yu,[2] and Xiaoji G. Xu*[1]

[1]Department of Chemistry, Lehigh University, 6 E Packer Ave., Bethlehem, PA, 18015, United States

[2]Department of Chemistry, Indiana University, 800 E Kirkwood Ave, Bloomington, IN, 47405, United States.

[1]Department of Chemistry, Lehigh University, 6 E Packer Ave., Bethlehem, PA, 18015, United States

[2]Department of Chemistry, Indiana University, 800 E Kirkwood Ave, Bloomington, IN, 47405, United States

*Corresponding Email: xgx214@lehigh.edu

ABSTRACT: Peak force infrared (PFIR) microscopy is an emerging atomic force microscopy that bypasses Abbe's diffraction limit in achieving chemical nano-imaging and spectroscopy. The PFIR microscopy mechanically detects the infrared photothermal responses in the dynamic tip-sample contact of peak force tapping mode, and has been applied for a variety of samples, ranging from soft matters, photovoltaics heterojunctions, to polaritonic materials under the air conditions. In this article, we develop and demonstrate the PFIR microscopy in the liquid phase for soft matters and biological samples. With the capability of controlling fluid compositions on demand, the liquid-phase peak force infrared (LiPFIR) microscopy enables *in situ* tracking the polymer surface reorganization in fluids and detecting the product of click chemical reaction in the aqueous phase. Both broadband spectroscopy and infrared imaging with ~ 10 nm spatial resolution are benchmarked in the fluid phase, together with complementary mechanical information. We also demonstrate the LiPFIR microscopy on revealing the chemical composition of a budding site of yeast cell wall particles in water as an application on biological structures. The label-free, non-destructive chemical nano-imaging and spectroscopic capabilities of the LiPFIR microscopy will facilitate the investigations of soft matters and their transformations at the solid/liquid interface.

While Abbe's diffraction limit restricts the spatial resolution of traditional infrared (IR) microscopy to half of the wavelength of several microns[1], sub-micron resolutions have been achieved in several super-resolution IR microscopy methods. For instance, in depth-resolving mid-infrared photothermal (MIP) microscopy, micromolar sensitivity and a spatial resolution of 600 nm were reported.[2-4] In ultraviolet-localized mid-infrared photoacoustic microscopy (ULM-PAM), high-throughput and water background-free images of cultured cells can be obtained with a diffraction-limited resolution of 250 nm.[5] However, the spatial resolution of these techniques is still diffraction-limited by the shortest wavelength involved in excitation or signal detection, which cannot be easily aligned down to <100 nm due to the limitation of the numerical aperture of IR objectives.

Integration of atomic force microscopy (AFM) with light radiation creates routes to achieve nanometer-scale spatial resolution far below the diffraction limit,[6, 7] thanks to the highly concentrated light field formed around the apex of the metallic tip. For example, vibrational imaging and Raman spectroscopy of single molecules have been achieved by the state-of-the-art tip-enhanced Raman scattering (TERS) with plasmonic enhancement.[8-11] For IR microscopy, current AFM-based IR spectroscopic imaging methods can be separated into two categories based on different detection schemes: optical detection through the elastic light scattering from the optical nearfield of the metallic tip;[7, 12] and mechanical detection of IR-induced actions between the sharp AFM tip and the sample as a result of light-matter interactions. The mechanical detection approach is particularly suitable for vibrational imaging and spectroscopy of soft matters, with high sensitivity and simple instrument design.[13-15] Photothermal induced resonance (PTIR),[16, 17] resonantly enhanced infrared photo-expansion nanoscopy (REINS),[18] photo-induced force microscopy (PiFM),[14] and peak force infrared (PFIR) microscopy[15] are increasingly popular representatives of AFM-based mechanical-detection IR methods, detecting IR signals directly proportional to sample's absorption profile. PTIR and REINS are based on the detection of the photothermal response from IR absorptions in the AFM contact mode operation.[13, 18] In contrast, PiFM, operating in the AFM tapping mode, detects the photo-induced force either of dipole-dipole origin,[19] optical-mechanical damping origin,[20] or photothermal expansions through modified van der Waals force.[21, 22] The PFIR microscopy, which operates with the peak force tapping mode (also known as the pulsed force mode),[23] combines the respective advantages of PTIR and PiFM. It achieves a high spatial resolution of < 10 nm and non-destructiveness to the sample surface like PiFM, and unambiguous photothermal signal generation mechanism like PTIR/REINS.

The PFIR microscopy also offers complimentary mechanical information channels, such as modulus and adhesion on the sample surface, allowing for simultaneous multimodal imaging together with the IR absorption.[15, 24]

On the flip side, a typical obstacle for IR microscopies is the lack of straightforward compatibility with aqueous conditions. Water strongly attenuates the IR radiation, making the delivery and detection of IR in traditional far-field microscopy extremely challenging. The utilization of total internal reflection could reduce the delivery loss of IR radiation. However, the spatial resolution of attenuated total internal reflection Fourier transform infrared (ATR-FTIR) microscopy is bound by the optical diffraction limit to several microns.[25] The AFM-based IR microscopies can address this challenge.[24, 26-31] With the total internal reflection geometry, evanescent IR field locally excites the vibrational modes of molecules and materials; the AFM tip probes the actions of the photothermal response excited by the evanescent field, avoiding the attenuation loss of the optical detection. REINS and contact mode PTIR have been demonstrated in the fluid phase on polymers and protein samples with a 20 ~ 25 nm spatial resolution.[26, 27] In addition, scattering-type scanning near-field optical microscopy (s-SNOM) with total internal reflection and bottom-up illumination have also been applied in water.[28, 29, 31] s-SNOM uses the optical detection scheme and is based on the tapping mode AFM that avoids scratching the sample surface by the tip. However, the optical detection scheme of the s-SNOM suffers from an additional loss from water absorption after the near-field scattering by the metallic tip. Moreover, the s-SNOM apparatus has a higher instrumental complexity and often requires two separate types of light

sources for IR imaging and spectroscopy. Recently, PiFM has also been implemented in the liquid,[32] however, the high hydraulic drag of the fluid damps the mechanical oscillations of the cantilever, reducing the efficiency for the heterodyne force detection scheme.[33]

Peak force tapping mode has been proven to operate stably in the liquid phase without sample damage for living cells[34] and single membrane proteins.[35] High-resolution AFM images of peak force tapping mode are routinely achieved in the liquid phase. PFIR microscopy inherits those advantages of peak force tapping for operations in liquids. Our group has developed liquid-phase peak force infrared (LiPFIR) microscopy by combining the photothermal detection mechanism of PFIR with the total internal reflection field delivery scheme. Imaging of phonon polaritons in hexagonal boron nitride submerged in water was demonstrated.[30] In this article, we further develop the LiPFIR microscopy with the ability to adjust the types of fluids on-demand to initiate physical transformations and chemical reactions. We first benchmark our LiPFIR microscopy by imaging nanoscale phase-separated polymer samples in water. Then, we utilize LiPFIR to monitor reaction sites of click chemistry on the polymer surface in solutions *in situ*, which demonstrates the capability of spectroscopically monitoring chemical reactions at the solid/liquid interface. From the sharp edge of a protein fibril, we also quantify the spatial resolution of LiPFIR microscopy to be ~ 10 nm. Finally, a biological sample of two zymosan particles in the budding process is imaged in water, revealing the presence of proteins around the budding site. These demonstrations prove that LiPFIR is generally suitable for label-free non-destructive chemical imaging of soft matters and
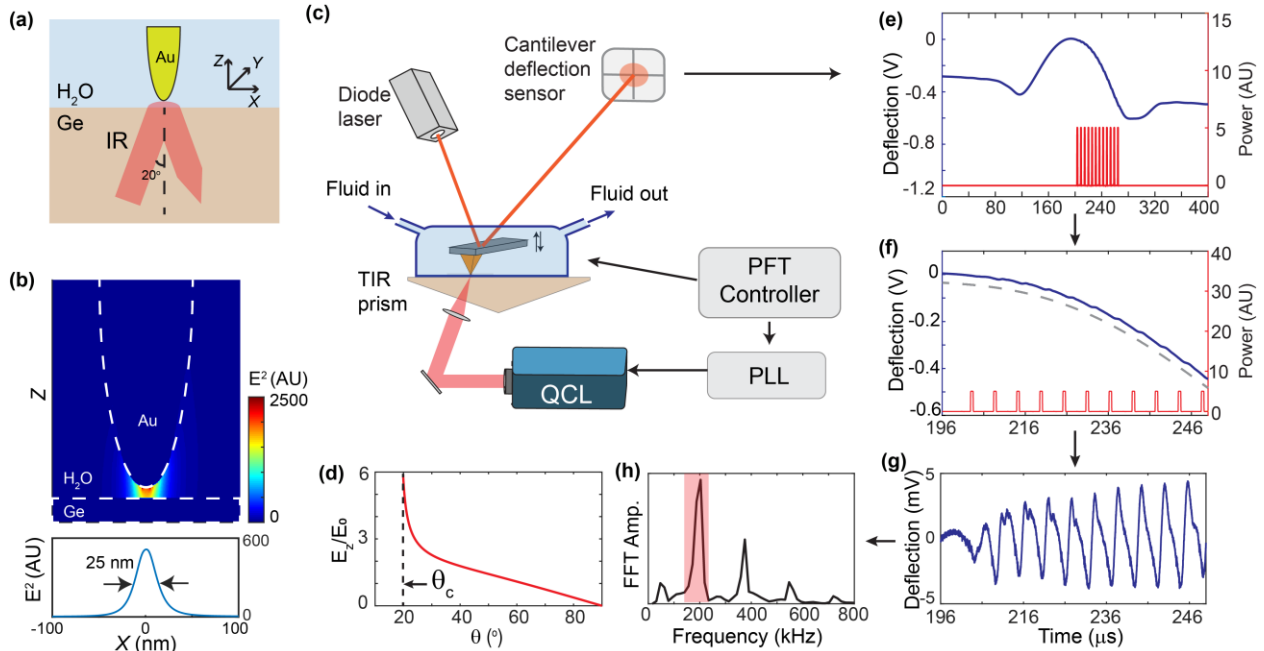

Figure 1. Design and operational principle of the LiPFIR microscope. (a) Scheme for total internal reflection. (b) FDTD simulation of the tip-enhanced evanescent field at the H$_2$O/Ge interface. The incident light is p-polarized (in-plane). The lower panel shows the field intensity across the Ge surface. (c) Apparatus of LiPFIR microscope. (d) The relative field strength of the evanescent infrared field at the Ge/water interface at different incident angles. The highest field strength is achieved at the critical angle, located at 19°. The wavelength used in the calculation is 6.25 μm. (e) The cantilever deflection signal of PFT in water (blue). The infrared pulse train (red) is synchronized to every PFT cycle. (f) Zoomed-in region of laser-induced cantilever oscillations (blue) and infrared pulse train (red). A polynomial fit is performed on the cantilever deflection to obtain a smooth background (gray dashed curve, offset from the original position for the comparison). (g) High-frequency oscillations of the cantilever. Subtracting the background from the cantilever deflection signal isolates high-frequency oscillations due to the laser-induced photothermal expansion. (h) Fast Fourier transform of (g). Usually, the strongest peak in FFT is integrated and used as the LiPFIR signal. (g) and (h) are experimentally obtained from single-frequency measurements.

solid/liquid interfacial processes, which should pave the way for more cutting-edge IR experiments in liquids with nanoscale spatial resolution.

Experimental

LiPFIR microscopy inherits the operational principle of PFIR microscopy[15] with the addition of total internal reflection delivery that overcomes the challenge of high attenuation of IR in water. The photothermal signal of the IR absorption is mechanically detected by the AFM cantilever, so the would-be propagation loss of the IR signal in the optical detection after the light-matter interaction is bypassed. Figure 1a illustrates the total internal reflection geometry used in the LiPFIR microscopy. The details of the apparatus is included in Supporting Information Note 1. An AFM tip (typically gold-coated) is placed above the germanium prism, and IR pulses are guided from the bottom at an incident angle of 20° to enable the total internal reflection. A finite-difference time-domain (FDTD) simulation of such a scheme is displayed in Figure 1b, where an intensity enhancement of 5.2×10^2 is achieved at the germanium surface underneath the AFM tip. Spatial confinement with the full width at half maximum (FWHM) of only 25 nm is observed, which is vital for AFM-based super-resolution imaging. This tip-enhanced field excites local sample molecules. The absorbed energy is then converted into photothermal expansions, which are mechanically detected by the motion of AFM cantilever. Peak force tapping (PFT) mode is used in LiPFIR. In PFT mode, the distance between the tip and sample oscillates at a low frequency of a few kHz. The tip momentarily contacts the sample surface for tens of microseconds and detaches afterward in every PFT cycle.[23, 36] The shear force that is built up in the lateral scan is released when the tip and the sample detach, avoiding the stick-slip motion of the contact mode AFM.[37] Unlike tapping mode AFM, the feedback of PFT is based on the maximal cantilever deflection during the tip-sample contact, which is not affected by the hydrodynamic drag force of the fluid.

Figure 1c illustrates the LiPFIR apparatus consisting of a frequency tunable IR source, a liquid-phase compatible AFM, and a germanium prism. A quantum cascade laser (QCL, MIRcat-QT, DRS Daylight Solutions) provides tunable IR laser pulses up to 1 μs duration with adjustable repetition rates. The beam from QCL is firstly expanded by a reflective telescope (BE04, Thorlabs) and then coupled into a germanium prism using a germanium lens with 2.5-cm focal length. A PFT-enabled AFM (Bioscope Catalyst, Bruker) operates on the germanium prism with a metal-coated probe and the PFT frequency of 1 kHz. A transistor to transistor logic (TTL) waveform from the phase lock loop (PLL) at the PFT frequency is routed to a function generator in the burst mode to trigger the QCL to emit a train of IR pulses. The timing of the emission is set to the moment when the tip and sample are in dynamic contact. The deflection of the cantilever is read out by a built-in quadrant photodiode in AFM. A perfusion chamber is sealed by an O-ring to enclose both the cantilever and the sample. The perfusion chamber has a fluid inlet and an outlet, enabling changing the fluid composition to initiate physical transformations and chemical reactions.

The calculated relationship between the Z-component of the evanescent field E_Z and the incident angle θ is plotted in Figure 1d.[38] As the incident angle approaches the critical angle $θ_c$ (which is calculated to be 19°), E_Z is significantly enhanced.[26] Note that the penetration depth is wavelength-dependent, which is larger for longer IR wavelengths. In practice, an incident angle of 21° is used in LiPFIR experiments, which is slightly
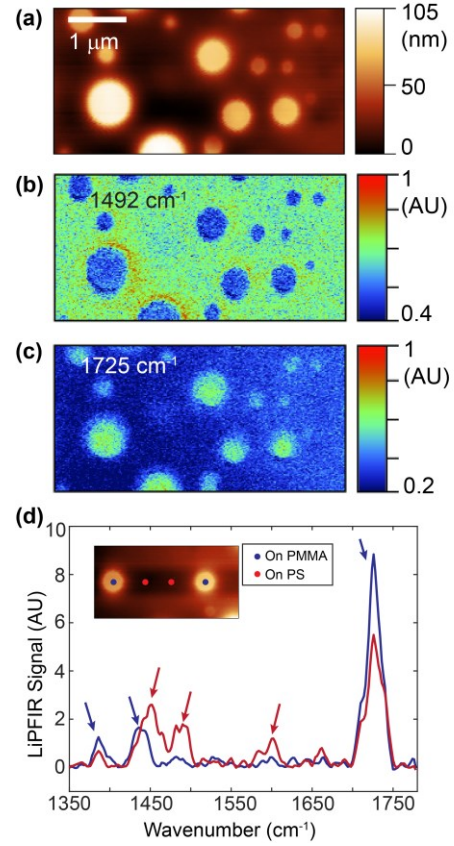

Figure 2. LiPFIR imaging and spectroscopy on PS:PMMA blend films. (a) AFM topography of a film of PS:PMMA blend in heavy water. (b-c) LiPFIR images at 1492 cm^{-1} (PS absorption) and 1725 cm^{-1} (PMMA absorption). (d) LiPFIR spectra collected from multiple locations on the PS:PMMA blend film. Inset shows the topography of a 3×1.5 μm² area, where measuring locations are labeled as point markers. Two measurements on each domain were made using the QCL increment of 2 cm^{-1} and averaged spectra are shown. Spectra are smoothed using third order Savitzky-Golay method with the span of 5. The baseline is removed. Characteristic PS and PMMA absorption peaks are indicated by red and blue arrows, respectively.

larger than the critical angle, and large enough to ensure total internal reflection for all mid-IR frequencies. As Figure 1b indicates, the metallic AFM tip further amplifies the evanescent field, and the laser-induced photothermal expansion will occur at a nanometre-size hotspot underneath the tip, providing a high spatial resolution.

Figure 1e shows an experimentally collected cantilever deflection curve that contains photothermal expansion signals caused by IR absorptions. The repetition rate of the pulse train is adjusted to maximize the oscillation amplitude of the cantilever from consecutive photothermal expansions, possibly due to the enhancement from matching the mechanical resonance of the cantilever. Figure 1f shows the zoomed-in region of the laser-induced oscillations. A polynomial fit (4th order) is performed to remove the slow varying curvature of the cantilever deflection in Figure 1f to retrieve pure oscillations at the repetition frequency of the laser pulse (Figure 1g). This procedure bypasses the self-reference scheme of the original PFIR microscopy,[15, 39] which doubles the signal acquisition speed. The amplitude of the cantilever oscillations is extracted by fast Fourier transform (FFT). The resulting peak corresponding to the laser repetition rate is integrated and used
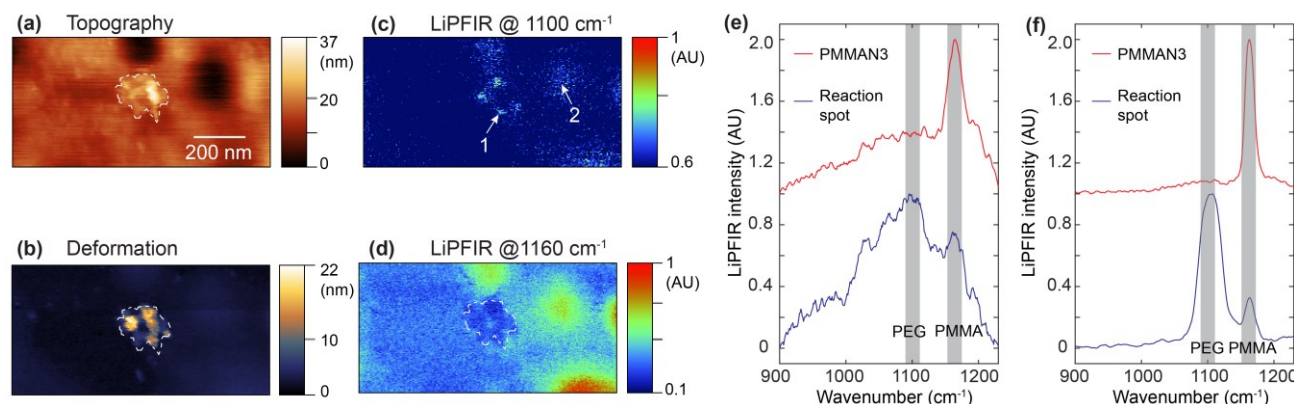
Figure 3. Revealing the click reaction site by LiPFIR. (a) Topography of the reaction site on the PMMA-N3 film. A protruded region can be observed and is enclosed by white dashed lines. (b) Deformation map of the same area from peak force tapping. (c-d) LiPFIR images at 1100 cm^{-1} and 1160 cm^{-1}, respectively. (e) Point spectra measured from the reaction spot (blue, position 1 in c) and the PMMA-N3 domain (red, position 2 in c). The spectra are leveled to remove the baseline. (f) Point spectra measured from the reaction spot and the PMMA-N3 domain in the air. The wavenumber increment used in spectra measurement is 1 cm^{-1}. The spectra are not leveled. In (e) and (f), three spectra are measured for each spot and the averaged results are smoothed using second order Savitzky-Golay method with the span of 11.

as the LiPFIR signal (Figure 1h). IR nano-imaging is achieved by scanning the AFM tip over the sample surface while registering the LiPFIR signal with a fixed laser frequency; nanospectroscopy is obtained by parking the AFM tip at a desirable location on the sample and sweeping the laser frequency from the QCL.

Results

Identification of Nanoscale Domains of Polymer Blends

Polymer blends formed by spontaneous phase separation serve as a model of soft matter to demonstrate the imaging and spectroscopy capability of LiPFIR microscopy. Figure 2a shows the topography of the polymer blend film (250-nm thick) formed by polystyrene (PS) and polymethyl methacrylate (PMMA) measured in heavy water. Two types of domains are noticeable in the topography: higher circular islands and a lower matrix region. Subjected to preparation conditions, spin-coated PS:PMMA blends can take different phase-separated geometries that cannot simply be distinguished from the topography. IR nano-imaging is required to perform chemical identification.

To do so, the incident laser of the LiFPIR microscopy is tuned to IR frequencies that correspond to vibrational resonances of PS and PMMA, respectively. The resulting IR images are displayed in Figure 2b-c. At 1492 cm^{-1}, PS domains exhibit a larger photothermal expansion signal as aromatic C=C bonds absorb strongly at this frequency. At 1725 cm^{-1}, PMMA domains are highlighted due to the absorption of the carbonyl C=O vibrations. Figures 2b-c allow chemical identification of the domain compositions of polymer submerged in the liquid phase: the higher islands in the PS:PMMA blend polymer film are PMMA domains, and the lower matrix is the PS domain.

Point spectra collected with LiPFIR are shown in Figure 2d. The raw data for each point measurement are provided in Supplementary Fig. S1. When the AFM tip is fixed on circular islands, the averaged spectrum shows IR signatures of PMMA. Besides a strong carbonyl absorption peak at 1725 cm^{-1}, there are also two peaks at 1380 cm^{-1} (α-methyl group vibration) and 1445 cm^{-1} (methyl C-H vibrations). In comparison, the averaged spectrum obtained from the PS domain shows absorption peaks at 1450 cm^{-1}, 1495 cm^{-1}, and 1601 cm^{-1}, all of which are from aromatic C=C vibrations of PS molecules. The distinctive spectra for PS and PMMA nanodomains indicate the

unambiguous chemical sensitivity of LiPFIR. Note that the carbonyl peak at 1725 cm^{-1} of PMMA is also present in the PS domain, which is likely caused by bulk absorption of PMMA. The same effect was also observed in PS-b-PMMA copolymers with standard air phase PFIR,[15] as well as in PiFM in the air.[14] These results demonstrate that LiPFIR is capable of distinguishing multi-component polymer domains through both IR imaging and spectroscopy. The signal-to-noise ratio (relative peak height divided by the standard deviation of the background) of the 1725 cm^{-1} peak of the untreated PMMA spectrum is calculated to be 74 (see Supplementary Fig. S2), which is comparable to the signal to noise ratio of 70 obtained on PMMA using PTIR in water without plasmonic enhancement.[27] As a demonstration of dynamic imaging in tracking the change of the absorption map in real time, we have also performed LiPFIR imaging in Supplementary Fig. S3 on monitoring surface reorganizations of PS:PMMA polymer domains induced by ethanol as the function of time, which exhibits the early stage of polymer swelling and delamination.

Investigation of Reaction Sites of Click Chemistry

Click chemistry offers a reliable way to synthesize chemicals with functional groups through the cycloaddition between azides and alkynes in water.[40] In click chemistry, one of the most common strategies is copper-catalyzed azide-alkyne cycloaddition (CuAAC), where copper(I) is utilized as the catalyst.[41] CuAAC has been utilized widely in organic synthesis,[41] polymer chemistry,[42] medical applications,[43] and bioconjugation labeling.[44] Spatially detecting the location of the CuAAC process at the nanoscale provides indications to the site-specific reactivity, which is important in heterogeneous materials and complex biological systems. Here, we utilize the LiPFIR microscopy to pinpoint reaction sites of the heterogeneous (solid/liquid) CuAAC in water.

Figure 3a illustrates the reaction process of the CuAAC between the azide-terminated PMMA (PMMA-N3) and the alkyne-functionalized biotin through polyethylene glycol chains (biotin-PEG-alkyne). The PMMA-N3 has a very similar absorptive profile to the regular PMMA in the range of 900 – 1800 cm^{-1}, and FTIR spectra of PMMA-N3 and regular PMMA are shown in Supplementary Fig. S4. Similar to the PS:PMMA blend mixture in Figure 2, PS:PMMA-N3 blend mixture is spin-
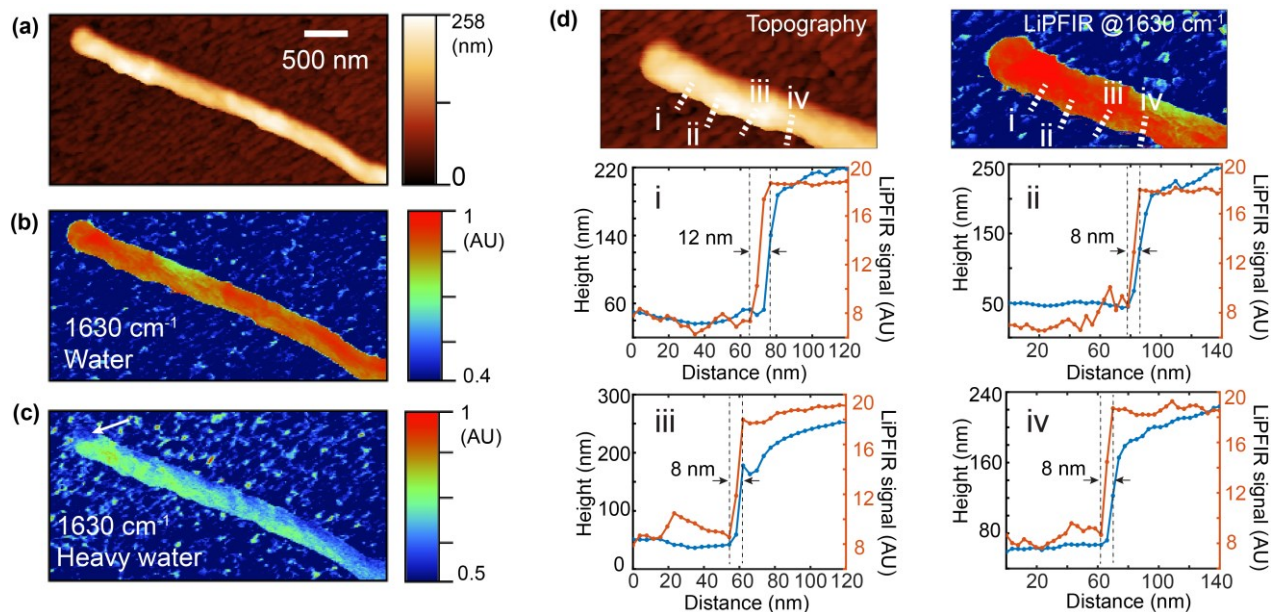
4

Figure 4. LiPFIR imaging of a BSA fibril in water and heavy water. (a) Topography of a 150-nm high and 350-nm wide BSA fibril. (b) Infrared images of the BSA fibril in aqueous 0.1×PBS solution at 1630 cm^{-1}. (c) Infrared images of the same BSA fibril in heavy water at 1630 cm^{-1}.(d) Height (blue curve) and LiPFIR signal (red curve) profiles from high-resolution topography and 1630 cm^{-1} infrared image of the BSA fibril in water. The pixel resolution is 3.9 nm. Four locations (i, ii, iii and iv) of the signal extraction are labeled as white dashed lines in the topography and infrared images. Spatial resolutions of 8-12 nm are estimated from the lateral distance between the signal maximum and minimum across the sharp edge of the fibril.

coated on the prism surface to form a solid polymer film, and its topography is shown in Supplementary Fig. S5a. Then, 40 μL of the reaction solution containing biotin-PEG-alkyne, $CuSO_4$ and $C_6H_7NaO_6$ is dropped on the polymer to start the CuAAC reaction. To examine the change of polymer morphology induced by the CuAAC, the prism surface is rinsed thoroughly with water after 90 min and air-dried. The polymer surface is then examined by the regular PFIR in the air in Supplementary Fig. S6. Several protrusions with lateral sizes less than 1 μm on the PMMA-N3 domains are found in the topography, which are proved to be CuAAC reaction sites through IR imaging and spectroscopy. The PFIR spectrum collected from one reaction site (indicated in Supplementary Fig. S5c-d) shown in Figure 3g exhibits a strong absorption peak of PEG at 1100 cm^{-1}, confirming the existence of biotin-PEG-alkyne at reaction sites. A full spectrum comparison performed in the air phase is provided in Supplementary Fig. S6e, where the amide I absorption of biotin is also observed.

Then, LiPFIR is used to locate the CuAAC reaction site in water *in situ*. After starting the reaction, the same sample area is scanned by LiPFIR intermittently without drying and LiPFIR images at 1100 cm^{-1} are captured. After 24 hours, a small protrusion area (~ 200 nm in diameter) is located on the PMMA-N3 domain in Figure 3b. In Figure 3c, the adhesion map shows this protrusion area has lower adhesion compared with that of adjacent PMMA-N3 domains. Figure 3d indicates four small bright spots at 1100 cm^{-1} around the protrusion area, while under the PMMA-N3 absorbing frequency of 1160 cm^{-1} in Figure 3e, these spots remain dark. Two point spectra displayed in Figure 3f are collected from one of four spots and unreacted PMMA-N3 surface nearby. A clear signature of PEG absorption at 1100 cm^{-1} is observed for the reaction site, while for the unreacted PMMA-N3, only the peak at 1160 cm^{-1} is present. The signal to noise ratio of the 1160 cm^{-1} peak for the PMMA-N3 domain in water is estimated to be 37 (see Supplementary

Fig. S7), which is smaller than that of 191 obtained on the PMMA-N3 domain in the air phase. From a cross-sectioning profile of one hotspot in Figure 3d, the detection limit of LiPFIR is estimated to be 1.2×10^3 biotin-PEG-alkyne molecules (Supplementary Fig. S8). While the air-phase PFIR provides the IR spectrum of the reaction product with excellent quality (Figure 3g), LiPFIR is capable of locating and distinguishing the CuAAC reaction site *in operando,* without drying the sample or interrupting the reaction. The joint usage of LiPFIR with CuAAC reaction will facilitate the biological investigations that use tags with click chemistry to pinpoint objects of interest at solid/liquid interface.

Quantification of Spatial Resolution of LiPFIR

Besides polymer samples, LiPFIR is also capable of imaging biological samples in water. Bovine serum albumin (BSA) has been widely utilized as a model protein to investigate a series of protein functions and applications. We use LiPFIR to perform nano-imaging of BSA fibrils in water. At room temperature, BSA proteins tend to form fibril structures in solution.[45, 46] To immobilize the BSA, the germanium surface is silanized with APTES (see Methods and Materials). AFM topography of a segment of a BSA fibril in 0.1×PBS buffer is shown in Figure 4a. This single BSA fibril is 150 nm in height and 350 nm in width. LiPFIR images at 1630 cm^{-1} (amide I band) are shown in Figure 4b-d in water and heavy water environments. In water, a large IR signal along the BSA fibril is observed, which distinguishes the protein fibril from the substrate. The spotty signals on the substrate are observed at small crevices formed on the rough germanium surface, where hot spots are created by strong field enhancements, leading to additional signal background from the photothermal expansion of the fluid. In heavy water, amide I band IR absorption is still present in the fibril. Another observation from Figure 4c is that a small region at the left terminal (indicated by an arrow) of the BSA fibril exhibits much reduced IR signal at 1630 cm^{-1}. Such a difference in IR
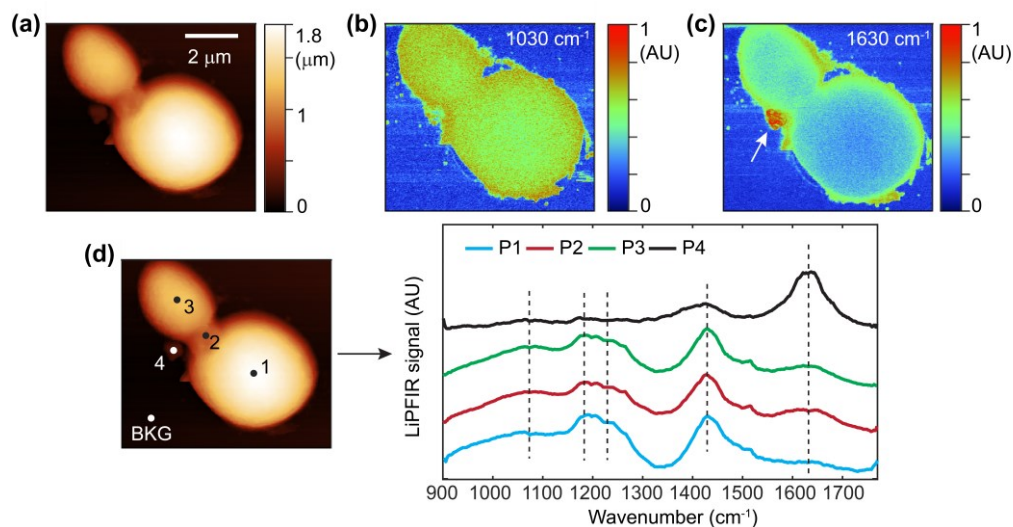
5

Figure 5. LiPFIR imaging and spectroscopy on zymosan particles. (a) Topography of two zymosan particles in heavy water. (b-c) LiPFIR images of two zymosan particles in heavy water at 1030 cm^{-1} and 1630 cm^{-1}, respectively. (d) The left panel indicates four spots of measurement for point spectra (positions 1 to 4). The position labeled by BKG is used to collect the background spectrum. The right panel shows collected spectra from four different locations on the two zymosan particles. Peaks at 1080, 1190, 1220, 1430 and 1630 cm^{-1} are labeled with dashed lines.

responses indicates a heterogeneous change of the protein secondary structure at the left terminal of the fibril when put in heavy water.

To estimate the spatial resolution of LiPFIR imaging, sectioned signal profiles from different locations of the edge of BSA fibril are plotted in Figure 3d, and spatial resolutions of 8 – 12 nm are obtained for LiPFIR in water. By comparison, contact mode AFM-IR in water recently achieved a 20 ~ 25 nm resolution,[26, 27] from a 100-nm spatial resolution in its early implementation.[16]

LiPFIR preserves the surface integrity of the sample during the measurement and allows for repeated measurements of the same region while changing the composition of the fluid. The topography of the BSA fibril stays the same after 8 hours of scans (Supplementary Fig. S9). The H-D exchange is revealed by spectroscopic results obtained *in situ* on the same location of BSA fibril in water and heavy water. Measured IR spectra are displayed in Supplementary Fig. S10. When in heavy water, since the majority of amide II band absorption is from N-H bonds in proteins, the replacement of N-H with N-D bonds redshifts the amide II absorption from 1550 to 1460 cm^{-1}.[47] As a result, a strong amide II band of the BSA fibril is observed in heavy water, which centers around 1460 cm^{-1} and indicates the completion of H-D exchange.

Investigating Yeast Budding Site in the Liquid Phase

Avoiding the destructive shear force means that the LiPFIR microscopy is suitable for imaging highly uneven soft matter samples with large height variations in water, such as biological cells. To demonstrate the capability of LiPFIR in imaging large and soft biological samples, we use it to examine the chemical composition of large cell wall particles derived from the yeast *Saccharomyces cerevisiae*. These cell wall particles are often referred to as zymosan particles, which represent a group of naturally occurring immunomodulators for therapeutic applications.[48-50]

Zymosan particles exhibit different shapes in the air and the aqueous phase. Supplementary Fig. S11a shows the topography of a dried zymosan particle in the air. The dried zymosan

particle exhibits a flattened disk-like shape with an average height of ~250 nm. In the dried form, the nucleus of the original yeast becomes noticeable and appears protruded from the center of the zymosan particle.[51, 52] Another noticeable feature on the zymosan particle is the presence of a bud scar. The bud scar is a ring-shaped fracture formed during the budding (division) process of yeast cells. We first perform air-phase peak force IR microscopy on this zymosan particle. The sample is illuminated at 1030 cm^{-1} (C-O-C vibrations) and 1630 cm^{-1} (amide I band), resolving the spatial distribution of polysaccharides and proteins spatially.[53] As shown in Supplementary Figs. S11b-c, the IR image at 1030 cm^{-1} suggests that polysaccharide components, which mainly included β-glucan and mannan, are evenly distributed across the zymosan surface. In comparison, the IR image at 1630 cm^{-1} clearly shows the uneven distribution of proteins. Proteins are enriched in multiple scattered spots, the nucleus, and the bud scar. Other locations of the zymosan particle also exhibit a small IR signal at 1630 cm^{-1}, indicating proteins are present together with polysaccharides on the rest area of the zymosan surface.

Dried zymosan particles, after immersed in heavy water, restore to their native ellipsoidal shape. Figure 5a shows the topography of two zymosan particles in heavy water with heights of more than 1 μm. The height of zymosan particles increases from 200~300 nm in the air to up to ~1.8 μm in heavy water, and the large nucleus observed in the air disappears because it is now enclosed inside the shell of the engorged zymosan particle. An unusual aspect of the AFM image of Figure 5d is that it captures two zymosan particles in the budding process with a septum formed in between. LiPFIR images are displayed in Figure 5b-c. In Figure 5e, an even distribution of polysaccharides is observed. In Figure 5f, the distribution of proteins also appears uniform, and slightly stronger signals present at peripherals because the evanescent IR field is stronger at lower heights from the Ge/water interface. Interestingly, strong 1630 cm^{-1} IR absorptions that correspond to amide I are observed on a cluster of material close to the budding site, as indicated by the arrow in Figure 5c. The cluster is connected with the budding septum from the bottom, as

6

revealed by the LiPFIR images. The measurement suggests that the septum in the budding process contains molecules of amide I band, e.g., protein or chitin.[54]

To further confirm the chemical composition of the cluster in the vicinity of the budding site, four point spectra are collected and shown in Figure 5d. Positions 1 and 3 are taken on the two zymosan particles, and position 2 is on the septum. Positions 1-3 show similar IR signatures of polysaccharides: The peak at 1190 cm^{-1} is attributed to the absorption of heavy water inside the zymosan particles; small IR absorptions between 1000~1100 cm^{-1} and the peak at 1220 cm^{-1} are due to the C-O stretching, and the peak at 1430 cm^{-1} is attributed to C-H bending. The spectrum collected on position 4, which is the bright spot observed at 1630 cm^{-1}, however, does not show discernable signatures of polysaccharide and chitin, which absorb around 1000~1100 cm^{-1}. Instead, a sole amide I band around 1630 cm^{-1} is observed. This finding confirms that the highlighted cluster observed at 1630 cm^{-1} is mainly composed of proteins, and a medium band around 1430 cm^{-1} is attributed to the H-D exchanged amide II band. The proteins in the cluster may participate in the synthesis of chitins during the budding process, as suggested by the literature.[55]

Discussion

The penetration depth of the evanescent field gives an upper boundary of the height of the sample that can be measured by the LiPFIR microscopy. The zymosan particles of Figure 5 are a high sample with a height of 1.8 μm. The penetration depth d of evanescent field established by the total internal reflection at the germanium/water interface can be calculated using the following equation:

$$d = \frac{\lambda}{4\pi\sqrt{n_1^2 \sin^2\theta - n_2^2}} \qquad (1)$$

where n_1 and n_2 are refractive indices of germanium and water, respectively, λ is light wavelength, and θ is the incident angle. With estimated values of $n_1 = 4$, $n_2 = 1.36$, $\lambda = 6.25$ μm, and $\theta = 20°$, Equation 1 gives a penetration depth of 3.3 μm, which is long enough to induce the tip-enhanced light field at the top of the zymosan particles.

The non-destructiveness of LiPFIR stems from the precise control of the maximal tip-sample forces in the PFT feedback. The lateral shear force between the AFM tip and sample is minimized in the PFT mode. The AFM tip only momentarily contacts with the sample surface for tens of μs in every PFT cycle. The shear force that is built up during the dynamic contact is released when the tip and sample detach in every PFT cycle. No large lateral shear force is accumulated. A direct comparison between the contact mode (where the lateral shear force is present) and peak force tapping mode in water is shown in Supplementary Fig. S12. Consecutive measurements with LiPFIR over an extended period (> 8 hours) on the protein fibrils do not induce any noticeable changes in the topography or disruptions of the sample surface (Supplementary Figure S9). In the zymosan studies of Figure 5, the zymosan particle filled with heavy water exhibit a height of 1.8 μm over a lateral dimension of 5 μm. The zymosan particle is also very soft, with a measured reduced Young's modulus of only 0.1 MPa in heavy water (Supplementary Figure S13). As an analogy, the zymosan in the liquid phase behaves like a water-filled balloon, and the nanoscopic AFM tip acts as a needle. Scratching the needle along the water-filled balloon would easily break it. Therefore, this is a type of sample that would be quite challenging for the contact mode AFM. The cantilever deflection setpoint should be very small to reduce the lateral force; the gain of the AFM feedback loop has to be large to cope with large height variations. However, a large feedback gain based on a low set point would amplify noise in the AFM scan, leading to possible sample damages when the AFM tip is out of topography feedback. In the LiPFIR, we use a high tapping amplitude of 100 nm and a low peak force setpoint of 1 nN to measure the zymosan sample, which provided stable topography feedback and adequate IR imaging.

The LiPFIR microscopy provides a spatial resolution of ~ 10 nm, which is slightly worse than the PFIR microscopy in the air phase.[53, 56] In comparison, the state-of-the-art resonantly enhanced contact mode AFM-IR techniques (i.e., REINS and resonantly enhanced PTIR) can achieve 20 ~ 25 nm spatial resolution in the liquid.[26, 27] LiPFIR gives a 2.5-time improved spatial resolution for liquid-phase IR microscopy, albeit at the expense of a lower signal strength than REINS or resonantly enhanced PTIR due to the fact that peak force tapping mode provides intermittently tip-sample contact, instead of constant contact in the contact mode. The improvement of spatial resolution of LiPFIR is due to the small area of contact in the peak force tapping when the peak force setpoint is kept low. The difference of mechanical properties across the composition boundary also improves the spatial contrast in the photothermal detection of IR absorption.

Recent development of total internal reflection scattering-type scanning near-field optical microscopy (s-SNOM) in the liquid achieves a spatial resolution of 30-80 nm.[28, 29] However, in order for s-SNOM to conveniently deliver IR imaging, a narrowband light source has to be used.[29] Furthermore, performing spectroscopy with narrowband light sources in s-SNOM for interferometric detection is time-consuming. To efficiently obtain IR imaging and spectroscopy for s-SNOM, both broadband and narrowband IR sources are often required.[31] In comparison, LiPFIR and other photothermal AFM-IR techniques can acquire both IR images and point spectra with only one set of frequency tunable narrowband laser source, also avoiding complex interferometric detection.

Conclusion

The compatibility with liquid-phase environments, the high spatial resolution, and the chemical sensitivity enables the LiPFIR microscopy to be a versatile platform for monitoring transformations at solid/liquid interfaces non-intrusively in a label-free manner. The LiPFIR microscope with the fluid perfusion chamber permits the nano-IR imaging and spectroscopy on spatial locations of interest under different liquid compositions that cause physical transformation and/or chemical reactions. This capability allows for *in situ* and *in operando* investigations over a broad range of solid/liquid interfacial chemical and biological processes, such as heterogeneous chemical reactions and catalysis,[57] polymer membranes for biofouling mitigation,[58] drug-protein interactions,[59] as well as chemical sensing through mid-IR polaritons.[24]

ASSOCIATED CONTENT

Supporting Information

The Supporting Information is available free of charge on the ACS Publications website. The Supporting Information includes supplementary Note 1. and supplementary Figures S1-S13.

AUTHOR INFORMATION

Corresponding Author

*xgx214@lehigh.edu

Author Contributions

X. G. X. designed the idea of LiPFIR. H.W. and X.G.X built the experimental apparatus. H.W. performed the numerical simulation, collected the data, and performed data analysis. Q. X. prepared the sample for the click reaction measurement. H.W., J. M. G., and X. G. X. wrote the manuscript. W. L. and Y. Y. provided the zymosan sample. X. G. X guided the overall research.

REFERENCES

1. Abbe, E., Beiträge zur Theorie des Mikroskops und der mikroskopischen Wahrnehmung. *Archiv für mikroskopische Anatomie* **1873,** *9* (1), 413-418.

2. Furstenberg, R.; Kendziora, C. A.; Papantonakis, M. R.; Nguyen, V.; McGill, R. In *Chemical imaging using infrared photothermal microspectroscopy*, Next-Generation Spectroscopic Technologies V, International Society for Optics and Photonics: 2012; p 837411.

3. Zhang, D.; Li, C.; Zhang, C.; Slipchenko, M. N.; Eakins, G.; Cheng, J.-X., Depth-resolved mid-infrared photothermal imaging of living cells and organisms with submicrometer spatial resolution. *Science Advances* **2016,** *2* (9), e1600521.

4. Li, Z.; Aleshire, K.; Kuno, M.; Hartland, G. V., Super-Resolution Far-Field Infrared Imaging by Photothermal Heterodyne Imaging. *The Journal of Physical Chemistry B* **2017,** *121* (37), 8838-8846.

5. Shi, J.; Wong, T. T. W.; He, Y.; Li, L.; Zhang, R.; Yung, C. S.; Hwang, J.; Maslov, K.; Wang, L. V., High-resolution, high-contrast mid-infrared imaging of fresh biological samples with ultraviolet-localized photoacoustic microscopy. *Nature Photonics* **2019,** *13* (9), 609-615.

6. Centrone, A., Infrared Imaging and Spectroscopy Beyond the Diffraction Limit. *Annual Review of Analytical Chemistry* **2015,** *8* (1), 101-126.

7. Richards, D.; Zayats, A.; Keilmann, F.; Hillenbrand, R., Near-field microscopy by elastic light scattering from a tip. *Philosophical Transactions of the Royal Society of London. Series A: Mathematical, Physical and Engineering Sciences* **2004,** *362* (1817), 787-805.

8. Zrimsek, A. B.; Chiang, N.; Mattei, M.; Zaleski, S.; McAnally, M. O.; Chapman, C. T.; Henry, A.-I.; Schatz, G. C.; Van Duyne, R. P., Single-Molecule Chemistry with Surface- and Tip-Enhanced Raman Spectroscopy. *Chemical Reviews* **2017,** *117* (11), 7583-7613.

9. Wang, X.; Huang, S.-C.; Huang, T.-X.; Su, H.-S.; Zhong, J.-H.; Zeng, Z.-C.; Li, M.-H.; Ren, B. J. C. S. R., Tip-enhanced Raman spectroscopy for surfaces and interfaces. **2017,** *46* (13), 4020-4041.

10. Mahapatra, S.; Li, L.; Schultz, J. F.; Jiang, N., Tip-enhanced Raman spectroscopy: Chemical analysis with nanoscale to angstrom scale resolution. *The Journal of Chemical Physics* **2020,** *153* (1), 010902.

11. Lipiec, E.; Kaderli, J.; Kobierski, J.; Riek, R.; Skirlińska-Nosek, K.; Sofińska, K.; Szymoński, M.; Zenobi, R., Nanoscale hyperspectral imaging of amyloid secondary structures in liquid. *Angewandte Chemie International Edition* **2020,** *n/a* (n/a).

12. Knoll, B.; Keilmann, F., Enhanced dielectric contrast in scattering-type scanning near-field optical microscopy. *Optics Communications* **2000,** *182* (4), 321-328.

13. Dazzi, A.; Prater, C. B., AFM-IR: Technology and Applications in Nanoscale Infrared Spectroscopy and Chemical Imaging. *Chemical Reviews* **2017,** *117* (7), 5146-5173.

14. Nowak, D.; Morrison, W.; Wickramasinghe, H. K.; Jahng, J.; Potma, E.; Wan, L.; Ruiz, R.; Albrecht, T. R.; Schmidt, K.; Frommer, J., Nanoscale chemical imaging by photoinduced force microscopy. *Science advances* **2016,** *2* (3), e1501571.

15. Wang, L.; Wang, H.; Wagner, M.; Yan, Y.; Jakob, D. S.; Xu, X. G., Nanoscale simultaneous chemical and mechanical imaging via peak force infrared microscopy. *Sci. Adv.* **2017,** *3* (6), e1700255.

16. Mayet, C.; Dazzi, A.; Prazeres, R.; Allot, F.; Glotin, F.; Ortega, J. M., Sub-100 nm IR spectromicroscopy of living cells. *Optics Letters* **2008,** *33* (14), 1611-1613.

17. Dazzi, A.; Prazeres, R.; Glotin, F.; Ortega, J. M., Local infrared microspectroscopy with subwavelength spatial resolution with an atomic force microscope tip used as a photothermal sensor. *Optics Letters* **2005,** *30* (18), 2388-2390.

18. Lu, F.; Jin, M.; Belkin, M. A., Tip-enhanced infrared nanospectroscopy via molecular expansion force detection. *Nature Photonics* **2014,** *8* (4), 307-312.

19. Almajhadi, M.; Wickramasinghe, H. K., Contrast and imaging performance in photo induced force microscopy. *Optics Express* **2017,** *25* (22), 26923-26938.

20. Almajhadi, M. A.; Uddin, S. M. A.; Wickramasinghe, H. K., Observation of nanoscale opto-mechanical molecular damping as the origin of spectroscopic contrast in photo induced force microscopy. *Nature Communications* **2020,** *11* (1), 5691.

21. Jahng, J.; Potma, E. O.; Lee, E. S., Tip-Enhanced Thermal Expansion Force for Nanoscale Chemical Imaging and Spectroscopy in Photoinduced Force Microscopy. *Analytical Chemistry* **2018,** *90* (18), 11054-11061.

22. Jahng, J.; Potma, E. O.; Lee, E. S., Nanoscale spectroscopic origins of photoinduced tip–sample force in the midinfrared. *Proceedings of the National Academy of Sciences* **2019,** *116* (52), 26359-26366.

23. Rosa-Zeiser, A.; Weilandt, E.; Hild, S.; Marti, O., The simultaneous measurement of elastic, electrostatic and adhesive properties by scanning force microscopy: pulsed-force mode operation. *Measurement Science and Technology* **1997,** *8* (11), 1333.

24. Jakob, D. S.; Wang, H.; Zeng, G.; Otzen, D. E.; Yan, Y.; Xu, X. G., Peak Force Infrared–Kelvin Probe Force Microscopy. *Angewandte Chemie International Edition* **2020,** *59* (37), 16083-16090.

25. Vongsvivut, J.; Pérez-Guaita, D.; Wood, B. R.; Heraud, P.; Khambatta, K.; Hartnell, D.; Hackett, M. J.; Tobin, M. J., Synchrotron macro ATR-FTIR microspectroscopy for high-resolution chemical mapping of single cells. *Analyst* **2019,** *144* (10), 3226-3238.

26. Jin, M.; Lu, F.; Belkin, M. A., High-sensitivity infrared vibrational nanospectroscopy in water. *Light: Science & Applications* **2017,** *6* (7), lsa201796.

27. Ramer, G.; Ruggeri, F. S.; Levin, A.; Knowles, T. P. J.; Centrone, A., Determination of polypeptide conformation with nanoscale resolution in water. *ACS Nano* **2018,** *12* (7), 6612-6619.

28. O'Callahan, B. T.; Park, K.-D.; Novikova, I. V.; Jian, T.; Chen, C.-L.; Muller, E. A.; El-Khoury, P. Z.; Raschke, M. B.; Lea, A. S., In Liquid Infrared Scattering Scanning Near-Field Optical Microscopy for Chemical and Biological Nanoimaging. *Nano Letters* **2020,** *20* (6), 4497-4504.

29. Pfitzner, E.; Heberle, J., Infrared Scattering-Type Scanning Near-Field Optical Microscopy of Biomembranes in Water. *The Journal of Physical Chemistry Letters* **2020,** *11* (19), 8183-8188.

30. Wang, H.; Janzen, E.; Wang, L.; Edgar, J. H.; Xu, X. G., Probing Mid-Infrared Phonon Polaritons in the Aqueous Phase. *Nano Letters* **2020,** *20* (5), 3986-3991.

31. Virmani, D.; Bylinkin, A.; Lopez, I. D.; Janzen, E.; Edgar, J. H.; Hillenbrand, R., Amplitude-and phase-resolved nano-imaging and nano-spectroscopy of polaritons in liquid environment. *arXiv preprint arXiv:2010.06229* **2020**.

32. Li, J.; Pang, J.; Yan, Z.-d.; Jahng, J.; Li, J.; Morrison, W.; Liang, J.; Zhang, Q.-Y.; Xia, X.-H., Antenna enhancing infrared photoinduced force imaging in aqueous environment with super-resolution and hypersensitivity. *arXiv preprint* **2020,** *arXiv:.11555*.

33. Cuberes, M. T.; Assender, H. E.; Briggs, G. A. D.; Kolosov, O. V., Heterodyne force microscopy of PMMA/rubber nanocomposites: nanomapping of viscoelastic response at ultrasonic frequencies. *Journal of Physics D: Applied Physics* **2000**, *33* (19), 2347.

34. Alsteens, D.; Dupres, V.; Yunus, S.; Latgé, J.-P.; Heinisch, J. r. J.; Dufrêne, Y. F., High-resolution imaging of chemical and biological sites on living cells using peak force tapping atomic force microscopy. *Langmuir* **2012**, *28* (49), 16738-16744.

35. Rico, F.; Su, C.; Scheuring, S., Mechanical mapping of single membrane proteins at submolecular resolution. *Nano Letters* **2011**, *11* (9), 3983-3986.

36. Pittenger, B.; Erina, N.; Su, C., Quantitative mechanical property mapping at the nanoscale with PeakForce QNM. *Application Note Veeco Instruments Inc.* **2010**, 1-12.

37. Johnson, K. L.; Woodhouse, J., Stick–slip motion in the atomic force microscope. *Tribology Letters* **1998**, *5* (2), 155-160.

38. Milosevic, M., On the nature of the evanescent wave. *Applied Spectroscopy* **2013**, *67* (2), 126-131.

39. Wang, L.; Wagner, M.; Wang, H.; Pau-Sanchez, S.; Li, J.; Edgar, J. H.; Xu, X. G., Revealing Phonon Polaritons in Hexagonal Boron Nitride by Multipulse Peak Force Infrared Microscopy. *Advanced Optical Materials* **2020**, *8* (5), 1901084.

40. Kolb, H. C.; Finn, M. G.; Sharpless, K. B., Click Chemistry: Diverse Chemical Function from a Few Good Reactions. *Angewandte Chemie International Edition* **2001**, *40* (11), 2004-2021.

41. Hein, J. E.; Fokin, V. V., Copper-catalyzed azide–alkyne cycloaddition (CuAAC) and beyond: new reactivity of copper(i) acetylides. *Chemical Society Reviews* **2010**, *39* (4), 1302-1315.

42. Meldal, M., Polymer "Clicking" by CuAAC Reactions. *Macromolecular Rapid Communications* **2008**, *29* (12-13), 1016-1051.

43. Geva-Zatorsky, N.; Alvarez, D.; Hudak, J. E.; Reading, N. C.; Erturk-Hasdemir, D.; Dasgupta, S.; von Andrian, U. H.; Kasper, D. L., In vivo imaging and tracking of host–microbiota interactions via metabolic labeling of gut anaerobic bacteria. *Nature Medicine* **2015**, *21* (9), 1091-1100.

44. McKay, Craig S.; Finn, M. G., Click Chemistry in Complex Mixtures: Bioorthogonal Bioconjugation. *Chemistry & Biology* **2014**, *21* (9), 1075-1101.

45. de la Arada, I.; Seiler, C.; Mäntele, W., Amyloid fibril formation from human and bovine serum albumin followed by quasi-simultaneous Fourier-transform infrared (FT-IR) spectroscopy and static light scattering (SLS). *European Biophysics Journal* **2012**, *41* (11), 931-938.

46. Pearce, F. G.; Mackintosh, S. H.; Gerrard, J. A., Formation of amyloid-like fibrils by ovalbumin and related proteins under conditions relevant to food processing. *Journal of Agricultural and Food Chemistry* **2007**, *55* (2), 318-322.

47. Blout, E.; De Loze, C.; Asadourian, A., The deuterium exchange of water-soluble polypeptides and proteins as measured by infrared spectroscopy. *Journal of the American Chemical Society* **1961**, *83* (8), 1895-1900.

48. Pan, Y.; Li, X.; Kang, T.; Meng, H.; Chen, Z.; Yang, L.; Wu, Y.; Wei, Y.; Gou, M., Efficient delivery of antigen to DCs using yeast-derived microparticles. *Scientific Reports* **2015**, *5*, 10687.

49. De Smet, R.; Demoor, T.; Verschuere, S.; Dullaers, M.; Ostroff, G. R.; Leclercq, G.; Allais, L.; Pilette, C.; Dierendonck, M.; De Geest, B. G., β-Glucan microparticles are good candidates for mucosal antigen delivery in oral vaccination. *Journal of Controlled Release* **2013**, *172* (3), 671-678.

50. Novak, M.; Vetvicka, V., β-glucans, history, and the present: immunomodulatory aspects and mechanisms of action. *Journal of Immunotoxicology* **2008**, *5* (1), 47-57.

51. Lombard, Y.; Giaimis, J.; Makaya-Kumba, M.; Fonteneau, P.; Poindron, P., A new method for studying the binding and ingestion of zymosan particles by macrophages. *Journal of Immunological Methods* **1994**, *174* (1-2), 155-165.

52. Jawhara, S.; Habib, K.; Maggiotto, F.; Pignede, G.; Vandekerckove, P.; Maes, E.; Dubuquoy, L.; Fontaine, T.; Guerardel, Y.; Poulain, D., Modulation of intestinal inflammation by yeasts and cell wall extracts: strain dependence and unexpected anti-inflammatory role of glucan fractions. *PloS One* **2012**, *7* (7).

53. Li, W.; Wang, H.; Xu, X. G.; Yu, Y., Simultaneous Nanoscale Imaging of Chemical and Architectural Heterogeneity on Yeast Cell Wall Particles. *Langmuir* **2020**, *36* (22), 6169-6177.

54. Fleet, G. H., Composition and structure of yeast cell walls. In *Current Topics in Medical Mycology*, Springer: 1985; pp 24-56.

55. Cabib, E.; Durán, A., Synthase III-dependent chitin is bound to different acceptors depending on location on the cell wall of budding yeast. *Journal of Biological Chemistry* **2005**, *280* (10), 9170-9179.

56. Jakob, D. S.; Wang, L.; Wang, H.; Xu, X. G., Spectro-Mechanical Characterizations of Kerogen Heterogeneity and Mechanical Properties of Source Rocks at 6 nm Spatial Resolution. *Analytical Chemistry* **2019**, *91* (14), 8883-8890.

57. Fechete, I.; Wang, Y.; Védrine, J. C., The past, present and future of heterogeneous catalysis. *Catalysis Today* **2012**, *189* (1), 2-27.

58. Gunari, N.; Brewer, L. H.; Bennett, S. M.; Sokolova, A.; Kraut, N. D.; Finlay, J. A.; Meyer, A. E.; Walker, G. C.; Wendt, D. E.; Callow, M. E.; Callow, J. A.; Bright, F. V.; Detty, M. R., The control of marine biofouling on xerogel surfaces with nanometer-scale topography. *Biofouling* **2011**, *27* (2), 137-149.

59. Ye, C.; Chi, H., A review of recent progress in drug and protein encapsulation: Approaches, applications and challenges. *Materials Science and Engineering: C* **2018**, *83*, 233-246.

Table of Contents artwork